**Astronomy
&
Astrophysics**

A semianalytical light curve model and its application to type IIP supernovae

A. P. Nagy[1], A. Ordasi[1], J. Vinkó[1,2], and J. C. Wheeler[2]

[1] Department of Optics and Quantum Electronics, University of Szeged, 6720 Szeged, Hungary
   e-mail: vinko@physx.u-szeged.hu
[2] Department of Astronomy, University of Texas at Austin, Austin, TX, USA

ABSTRACT

The aim of this work is to present a semianalytical light curve model code that can be used for estimating physical properties of core collapse supernovae (SNe) in a quick and efficient way. To verify our code we fit light curves of Type II SNe and compare our best parameter estimates to those from hydrodynamical calculations. For this analysis, we use quasi-bolometric light curves of five different Type IIP SNe. In each case, we obtain appropriate results for initial pre-supernova parameters. We conclude that this semianalytical light curve model is useful to obtaining approximate physical properties of Type II SNe without using time-consuming numerical hydrodynamic simulations.

Key words. supernovae: general

1. Introduction

The light curves of Type IIP supernovae (SNe) are characterized by a plateau phase with a duration of about 80–120 days and a quasi-exponential tail caused by the radioactive decay of ^{56}Co (e.g., Maguire et al. 2010). The emitted flux at later phases is directly determined by the mass of ejected ^{56}Ni. Besides nickel mass, other parameters specify the bolometric luminosity of SNe, such as explosion energy, ejected mass, and the initial size of the radiating surface (Grassberg et al. 1971; Litvinova & Nadyozhin 1985). The radius of this surface is thought to be equal to the radius of the progenitor at the moment of shock breakout following core collapse.

A general approach to determine the properties of supernova explosions is the modeling of observed data with hydrodynamical codes (Grassberg et al. 1971; Falk & Arnett 1977; Hillebrandt & Müller 1981; Blinnikov et al. 2000; Nadyozhin 2003; Utrobin et al. 2007; Pumo et al. 2010; Bersten et al. 2011). However, a simple analytical method may also be used to obtain approximate results (Arnett 1980, 1982; Zampieri et al. 2003; Chatzopoulos et al. 2012). With the help of these analytic light curve models, the basic physical parameters, such as explosion energy, ejected mass and initial radius, can be estimated (Arnett 1980; Popov 1993). Although such simple estimates can be considered only preliminary, they can be obtained without running complicated, time-consuming hydrodynamical simulations. Analytic codes may be useful in providing constraints for the most important physical parameters, which can be used as input in more detailed simulations. Also, analytic codes may also give first-order approximations when observational information is limited, for example, when only photometry and no spectroscopy is available for a particular SN.

In this paper we describe a semianalytical light curve model, which is based on the model originally developed by Arnett & Fu (1989). We assume a homologously expanding and spherically symmetric SN ejecta have a uniform density core and an exponential density profile in the other layers. Radiation transport is treated by the diffusion approximation. The effect of recombination causing the rapid change of the effective opacity in the envelope is taken into account in a simple form introduced by Arnett & Fu (1989).

This paper is organized as follows: in Sect. 2, we describe the model and its implementation, and also present the effect of variations of the initial input parameters on the calculated bolometric luminosity. In Sect. 3, we compare the results obtained for SN 2004et, SN 2005cs, SN 2009N, SN 2012A, and SN 2012aw from our code and several hydrodynamic computations. Finally, Sect. 4 summarizes the main results of this paper.

2. Main assumptions and model parameters

2.1. The light curve model

We adopt the radiative diffusion model originally developed by Arnett (1980) and modified by Arnett & Fu (1989) to take the effect of the recombination front in the ejecta into account. Below we review the original derivation, and present some corrections and implementations for numerical computations.

The first law of thermodynamics in Lagrangian coordinates for a spherical star may be written as

$$\frac{\mathrm{d}E}{\mathrm{d}t} + P\frac{\mathrm{d}V}{\mathrm{d}t} = \epsilon - \frac{\partial L}{\partial m}, \tag{1}$$

where E is the internal energy per unit mass, P is the pressure, $V = 1/\rho$ is the specific volume, ϵ is the entire energy production rate per unit mass, and L is the luminosity (Arnett 1980, 1982). In a radiation-dominated envelope, the internal energy per unit mass is $E = a\,T^4 V$ and the pressure is $P = E/3V$, where a is the radiation density constant. The energy loss is driven by

photon diffusion, so we may use the following equation for the derivative of the luminosity:

$$\frac{\partial L}{\partial m} = \frac{1}{4\pi r^2 \rho} \frac{\partial L}{\partial r} = -\frac{a}{r^2 \rho} \frac{\partial}{\partial r}\left(\frac{c\, r^2}{3\kappa \rho} \frac{\partial T^4}{\partial r}\right), \tag{2}$$

where κ is the mean opacity, T is the temperature, and ρ is the density. Since the supernova ejecta expand homologously we define a comoving, dimensionless radius x as

$$r = R(t) \cdot x, \tag{3}$$

where r is the distance of a particular layer from the center and $R(t)$ is the total radius of the expanding envelope at a given time. In the comoving coordinate system, we are able to separate the time and space dependence of the physical properties. Thus, the density profile can be described as

$$\rho(x,t) = \rho(0,0)\, \eta(x) \left(\frac{R_0}{R(t)}\right)^3, \tag{4}$$

where R_0 is the initial radius and $\eta(x) \sim \exp(-\alpha x)$ where α is assumed to be a small positive integer. The time-dependent term describes the dilution of the density due to expansion.

The ejecta are expected to be fully ionized shortly after the explosion, so it seems reasonable to consider a recombination front that moves inward through the envelope. The assumed recombination wave divides the ejecta into two different parts. The boundary separating the two layers occurs at the dimensionless radius x_i where the local temperature $T(x)$ drops below the recombination temperature $T_{\rm rec}$. Inside this recombination radius, the ejecta are assumed to be fully ionized. The opacity (κ) changes strongly at the boundary layer separating the two parts. Because the opacity has a strong nonlinear dependence on the temperature, we assume a simple step-function to approximate its behavior (Arnett & Fu 1989):

$$\kappa(x,t) = \begin{cases} \kappa_t, & \text{if } T(x) \geq T_{\rm rec} \\ 0, & \text{if } T(x) < T_{\rm rec} \end{cases} \tag{5}$$

where $T_{\rm rec}$ is the recombination temperature, below which the ejecta are mostly neutral. In this approximation, we use the Thomson-scattering opacity for pure hydrogen gas as $\kappa \sim 0.4\ {\rm cm^2/g}$, and model the presence of heavier elements by setting κ to lower values. For example, $\kappa \sim 0.2\ {\rm cm^2/g}$ is assumed for a He-dominated ejecta, while for a He-burned atmosphere κ may be $\sim 0.1\ {\rm cm^2/g}$.

Following Arnett (1980), the temperature evolution and its spatial profile can be approximated as

$$T^4(x,t) = T^4(0,0)\, \psi(x)\, \phi(t) \left(\frac{R_0}{R(t)}\right)^4. \tag{6}$$

and the radial components of this function is

$$\psi(x) \approx \frac{\sin(\pi x)}{\pi x}, \tag{7}$$

which does not change during the expansion. While implementing the temperature profile in our C-code, we found that the direct application of the $\sin(x)$ function caused numerical instabilities due to rounding errors around $x \approx 1$. To reduce this problem, we used a 4th order Taylor-series expansion of the $\psi(x)$ function (see Fig. 1). The implementation of the Taylor-series approximation increased the numerical stability when computing the effect of recombination.
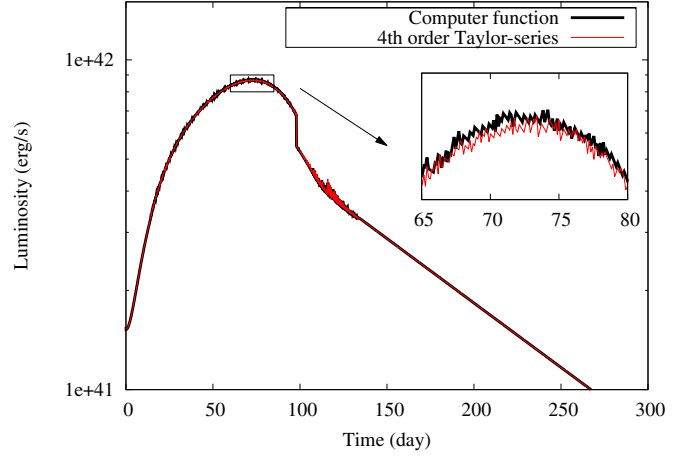
Fig. 1. Model light curve computed with exact $\sin(\pi x)/(\pi x)$ temperature profile (black) and with 4th order Taylor series (red).

Another important physical quantity is the energy production rate, which can be defined as

$$\epsilon(x,t) = \epsilon(0,0)\, \xi(x)\, \zeta(t). \tag{8}$$

In this case, a central energy production is assumed, which means that $\xi(x)$ is the Dirac-delta function at $x = 0$. The temporal dependence of the $\epsilon(t)$ function was specified by assuming either radioactive decay or magnetar-controlled energy input. In the following subsections we summarize these two different conditions.

2.1.1. Radioactive energy input

In this case only the radioactive decay of ^{56}Ni and ^{56}Co supplies the input energy. In such a model $\epsilon(0,0)$ is equal to the initial energy production rate of ^{56}Ni-decay. The time-dependent part of the $\epsilon(x,t)$ function, when the ejecta are optically thick for gamma-rays, is given by

$$\zeta(t) = X_{\rm Ni} + \frac{\epsilon_{\rm Co}}{\epsilon_{\rm Ni}} X_{\rm Co}, \tag{9}$$

where $X_{\rm Ni}$ and $X_{\rm Co}$ are the number of nickel and cobalt atoms per unit mass, respectively, $\epsilon_{\rm Ni}$ and $\epsilon_{\rm Co}$ are the energy production rate from the decay of these elements. The number of the radioactive elements varies as

$$\frac{{\rm d}X_{\rm Ni}}{{\rm d}z} = -X_{\rm Ni} \quad \text{and} \quad \frac{{\rm d}X_{\rm Co}}{{\rm d}z} = X_{\rm Ni} - \frac{\tau_{\rm Ni}}{\tau_{\rm Co}} X_{\rm Co}, \tag{10}$$

where $z = t/\tau_{\rm Ni}$ is the dimensionless timescale of the Ni-Co decay, $\tau_{\rm Ni}$ and $\tau_{\rm Co}$ are the decay time of nickel and cobalt, respectively.

The comoving coordinate of the recombination front is denoted as x_i. Following Arnett & Fu (1989) it is assumed that the radiative diffusion takes place only within x_i where $\kappa > 0$, and the photons freely escape from $x = x_i$. Thus, the surface at x_i acts as a pseudo-photosphere.

After inserting the quantities defined above into Eq. (1), we have

$$\frac{{\rm d}E}{{\rm d}t} + P\frac{{\rm d}V}{{\rm d}t} = \frac{a\, T^4(x,t)\, x_i^3\, V}{\phi(t)} \frac{{\rm d}\phi(t)}{{\rm d}t} + 2\, a\, T^4(x,t)\, x_i^2\, V\, \frac{{\rm d}x_i}{{\rm d}t}. \tag{11}$$

Now, applying the assumption made by (Arnett 1982, see his Eq. (13)), the temporal and spatial parts of Eq. (11) can be separated, thus, both of them are equal to a constant (the "eigenvalue" of the solution). After separation, the equation describing the temporal evolution of the $\phi(t)$ function can be expressed as

$$\frac{\mathrm{d}\phi(t)}{\mathrm{d}t}\,\tau_{\mathrm{Ni}} = \frac{R(t)}{R_0\,x_i^3}\left[p_1\zeta(t) - p_2\,x_i\,\phi(t) - 2\,\tau_{\mathrm{Ni}}\,x_i^2\,\phi(t)\frac{R_0}{R(t)}\frac{\mathrm{d}x_i}{\mathrm{d}t}\right], \quad (12)$$

where we corrected a misprint that occurred in Eq. (A41) of Arnett & Fu (1989). This equation contains two parameters defined as

$$p_1 = \frac{\tau_{\mathrm{Ni}}\epsilon_{\mathrm{Ni}}M_{\mathrm{Ni}}^0}{E_{\mathrm{Th}}(0)} \quad \text{and} \quad p_2 = \frac{\tau_{\mathrm{Ni}}}{\tau_{\mathrm{d}}}, \quad (13)$$

where $M_{\mathrm{Ni}}^0 = 4\pi\rho(0,0)R_0^3\int_0^1\xi(x)\eta(x)x^2\mathrm{d}x$ and $E_{\mathrm{Th}}(0) = 4\pi R_0^3 aT^4(0,0)\int_0^1\psi(x)x^2\mathrm{d}x$ are the initial total nickel mass and the initial thermal energy, respectively.

Equation (12) was solved by the Runge-Kutta method with the approximation of $\mathrm{d}x_i/\mathrm{d}t \approx \Delta x_i/\Delta t$, where a small time-step of $\Delta t = 1$ s was applied. In the nth time-step $\Delta x_i = x_i^{(n)} - x_i^{(n-1)}$ was used, where $x_i^{(n)}$ and $x_i^{(n-1)}$ are the dimensionless radii of the recombination layer in the nth and $(n-1)$th time-step, respectively. To determine the value of $x_i^{(n)}$ in every time-step, our code divides the envelope into thin ($\delta x = 10^{-9}$) layers, then calculates the temperature in each layer starting from the outmost layer at $x = 1$ until the temperature exceeds the recombination temperature T_{rec}. If that occurs at the kth layer then $x_i \approx (x_k + \delta x/2)$ is chosen as the new radius of the recombination layer.

Finally, the total bolometric luminosity can be expressed as a sum of the radioactive heating plus the energy released by the recombination:

$$L(t) = x_i\frac{\phi(t)\,E_{\mathrm{Th}}(0)}{\tau_{\mathrm{d}}} + 4\,\pi\,r_i^2\,Q\,\rho(x_i,t)\frac{\mathrm{d}r_i}{\mathrm{d}t}, \quad (14)$$

where $\tau_{\mathrm{d}} = 3\,\kappa\,\rho(0,0)\,R_0^2/(\pi^2 c)$ is the diffusion timescale, and $Q = 1.6\times10^{13}(Z/A)Z^{4/3}$ is the recombination energy per unit mass. The effect of gamma-ray leakage can be taken into account as

$$L(t) = x_i\frac{\phi(t)\,E_{\mathrm{Th}}(0)}{\tau_{\mathrm{d}}}\left(1 - \mathrm{e}^{-A_g/t^2}\right) + 4\,\pi\,r_i^2\,Q\,\rho(x_i,t)\frac{\mathrm{d}r_i}{\mathrm{d}t}, \quad (15)$$

where the A_g factor refers to the effectiveness of gamma-ray trapping. The optical depth of gamma rays can be defined as $\tau_g = A_g/t^2$ (Chatzopoulos et al. 2012). This parameter is significant in modeling the light curves of Type IIb and Ib/c SNe.

2.1.2. Magnetar spin-down

Magnetars represent a subgroup of neutron stars with a strong (10^{14}–10^{15} G) magnetic field. The spin-down power of a newly formed magnetar can create a brighter and faster evolving SN light curve than radioactive decay (Piro & Ott 2011). This mechanism can contribute to the extreme peak luminosity of Type Ib/c and super-luminous SNe (Woosley 2010; Kasen & Bildsten 2010; Chatzopoulos et al. 2012).

In this case, $\epsilon(t)$ includes radioactive energy production as well as magnetar spin-down:

$$\epsilon(t) = \epsilon_{\mathrm{Ni}}(t) + \epsilon_M(t), \quad (16)$$

Table 1. Comparison of magnetar model peak luminosities with the analytic estimates.

E_{p} (10^{51} erg)	t_{p} (day)	$L_{\mathrm{peak}}^{\mathrm{ref}}$ (10^{44} erg/s)	$L_{\mathrm{peak}}^{\mathrm{model}}$ (10^{44} erg/s)
1	5	1.76	1.94
5	2	7.09	7.98
5	5	8.81	9.71
5	10	8.61	9.79
5	50	4.15	5.89
10	5	17.6	19.4

where $\epsilon_{\mathrm{Ni}}(t)$ is the energy production rate of radioactive decay of nickel and cobalt as defined in the previous section and $\epsilon_M(t)$ is the energy production rate of the spin-down per unit mass. The power source of the magnetar is given by the spin-down formula

$$\epsilon_M(t) = \frac{E_{\mathrm{p}}}{t_{\mathrm{p}}\,M_{\mathrm{ej}}}\frac{l-1}{(1+t/t_{\mathrm{p}})^l}, \quad (17)$$

where M_{ej} is the ejected mass, E_{p} is the initial rotational energy of the magnetar, t_{p} is the characteristic timescale of spin-down, which depends on the strength of the magnetic field, and $l = 2$ for a magnetic dipole.

Solving Eq. (1) as in the previous section the $\phi(t)$ function can be expressed as

$$\frac{\mathrm{d}\phi(t)}{\mathrm{d}t}\,\tau_{\mathrm{Ni}} = \frac{R(t)}{R_0\,x_i^3}\left[p_1\zeta(t) - p_2\,x_i\,\phi(t) + p_3\frac{1}{(1+t/t_{\mathrm{p}})^2}\right] - 2\tau_{\mathrm{Ni}}\,\phi(t)\frac{1}{x_i}\frac{\mathrm{d}x_i}{\mathrm{d}t}, \quad (18)$$

where $p_3 = \tau_{\mathrm{Ni}}E_{\mathrm{p}}/E_{\mathrm{Th}}(0)t_{\mathrm{p}}$. The total bolometric luminosity in this configuration is calculated using Eqs. (14), (15) with the numerical integration of the modified $\phi(t)$ function.

To verify the magnetar model, we compared our results with the estimated peak luminosities defined by Kasen & Bildsten (2010):

$$L_{\mathrm{peak}}^{\mathrm{ref}} \approx \frac{E_{\mathrm{p}}\,t_{\mathrm{p}}}{t_{\mathrm{d}}^2}\left[\ln\left(1 + \frac{t_{\mathrm{d}}}{t_{\mathrm{p}}}\right) - \frac{t_{\mathrm{d}}}{t_{\mathrm{d}} + t_{\mathrm{p}}}\right], \quad (19)$$

where t_{d} is the effective diffusion timescale (Arnett 1980):

$$t_{\mathrm{d}} = \sqrt{\frac{2\,\kappa\,M_{\mathrm{ej}}}{13.8\,v_{\mathrm{sc}}\,c}} \quad (20)$$

and $v_{\mathrm{sc}} \approx \sqrt{10E_{\mathrm{SN}}/3M_{\mathrm{ej}}}$ is the characteristic ejecta velocity.

For the test case, we used the following fixed parameters: $R_0 = 5\times10^{11}$ cm; $M_{\mathrm{ej}} = 1\,M_\odot$; $M_{\mathrm{Ni}}^0 = 0\,M_\odot$; $T_{\mathrm{rec}} = 0$ K (i.e., no recombination); $E_{\mathrm{kin}}(0) = 3$ foe (1 foe $= 10^{51}$ erg); $E_{\mathrm{Th}}(0) = 2$ foe; $\alpha = 0$ (constant density model); $\kappa = 0.34$ cm^2/g; $A_g = 10^6$ day^2 (full gamma-ray trapping). These parameters imply $v_{\mathrm{sc}} \sim 22\,400$ km s^{-1} and $t_{\mathrm{d}} \sim 14$ days. Values of E_{p} and t_{p} were varied within a range typical for magnetars (Kasen & Bildsten 2010). Table 1 shows the peak luminosities estimated from the formulae above ($L_{\mathrm{peak}}^{\mathrm{ref}}$) and provided by our code ($L_{\mathrm{peak}}^{\mathrm{model}}$). We found acceptable agreement between the calculated and the model values, although the analytic formula slightly underestimates the model peaks.

2.2. The effect of varying input parameters

To create light curves we need to integrate Eqs. (12)–(18) then apply Eqs. (14), (15) in every time-step. The input parameters for the model are the following:

- R_0: initial radius of the ejecta (in 10^{13} cm);
- M_{ej}: ejected mass (in $M_\odot$);
- M_{Ni}^0: initial nickel mass (in $M_\odot$);
- T_{rec}: recombination temperature (in K);
- $E_{kin}(0)$: initial kinetic energy (in foe);
- $E_{Th}(0)$: initial thermal energy (in foe);
- α: density profile exponent ;
- κ: opacity (in cm^2/g);
- E_p: initial rotational energy of the magnetar (in foe);
- t_p: timescale of magnetar spin-down (in day); and
- A_g: gamma-ray leakage exponent (in day^2).

We tested our code by changing these input parameters and comparing the resulting light curves to those of Arnett & Fu (1989). The parameters were varied one by one using three different values while holding the others constant. The following reference parameters were chosen (plotted with black): $R_0 = 5 \times 10^{12}$ cm; $M_{ej} = 10\ M_\odot$; $M_{Ni}^0 = 0.01\ M_\odot$; $T_{rec} = 6000$ K; $E_{kin}(0) = 1$ foe; $E_{Th}(0) = 1$ foe; $\alpha = 0$; $\kappa = 0.3\ cm^2/g$; $E_p = 0$ foe; $t_p = 0$ days; $A_g = 10^6\ day^2$. When the magnetar energy input was taken into account the two characteristic parameters were $E_p = 1$ foe and $t_p = 10$ days.

First, we created light curves with three different radii: 5×10^{11}, 5×10^{12}, and 5×10^{13} cm. As seen in Fig. 2a, the modification of this parameter mainly influences the early part of the light curve. As a result of the increasing radius, the peak of the light curve becomes wider and flatter. The rapid decline after the plateau also becomes steeper. As Type IIP SNe exhibit steep declines after the plateau phase, this behavior is consistent with their larger progenitor radii. Our code replicates this behavior.

Next, we set 5, 10, and 15 $M_\odot$ as the three input values of the ejected mass. This parameter also affects the maximum and the width of the light curve (Fig. 2b). Higher ejecta masses result in lower peak luminosities and more extended plateau phases.

The three different values of nickel mass were 0.001, 0.01, and 0.1 $M_\odot$. Figure 2c shows the strong influence of this parameter on all phases of the light curve. Increasing nickel mass causes a global increase of the luminosity at all phases, as expected. This panel also illustrates that the late-phase luminosity level depends on only the Ni-mass in the case of full gamma-ray trapping.

Figure 2d shows the effect of the modification of the recombination temperature from 5000 K to 7000 K. This parameter has no major influence on the light curve. Higher T_{rec} results in a shorter plateau phase and the short decline phase after the plateau also becomes steeper. The recombination temperature is the parameter that can be used to take the ejecta chemical composition into account. For example, the recombination temperature for pure H ejecta is ~5000 K, but for He-dominated ejecta it is higher, $T_{rec} \sim 7000$ K (Grassberg & Nadyozhin 1976), or $T_{rec} \sim 10\,000$ K (Hatano et al. 1999).

One of the most important parameters of SN events is the explosion energy (E_{SN}), which is the sum of the kinetic and the thermal energy. In this work, we examined the effect of these two parameters separately. The three values of the kinetic energy were 0.5, 1, and 5 foe. As Fig. 3a shows, this parameter has significant influence on the shape of the early light curve, but
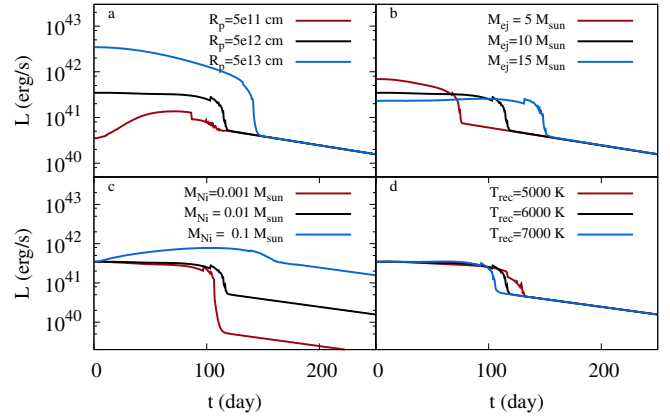
Fig. 2. Effect of changing the initial radius of the ejecta (panel **a**)), the ejected mass (panel **b**)), the initial nickel mass (panel **c**)), and the recombination temperature (panel **d**)).
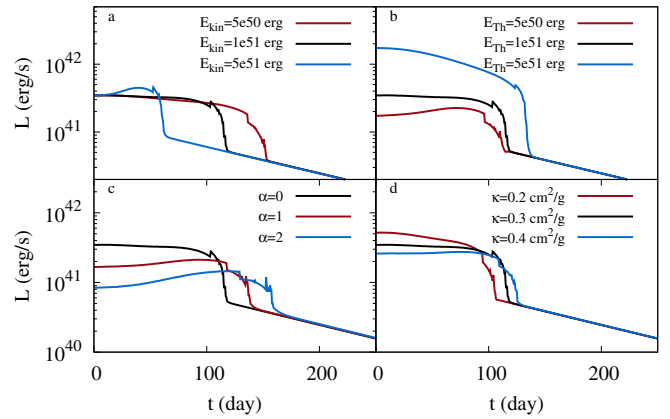

Fig. 3. Effect of changing the initial kinetic energy (panel **a**)), the initial thermal energy (panel **b**)), the density profile exponent (panel **c**)), and the opacity (panel **d**)).

does not have any effect on the late part because, again, the luminosity at late phases are set by only the initial Ni-mass. When the kinetic energy is lower, the plateau becomes wider, while the maximum luminosity decreases. Note that using extremely high kinetic energy results in the lack of the plateau phase. The influence of the thermal energy is somewhat similar: it mainly affects the early light curve (Fig. 3b). Increasing thermal energy widens the plateau, and the peak luminosity rises. For high E_{Th} the plateau phase starts to disappear, just as for high E_{kin}.

The density profile exponent was chosen as 0, 1, and 2. Figure 3c. shows that the different values cause changes mainly in the maximum of the light curve and the duration of the plateau phase. If the density profile exponent is higher, then the luminosity is reduced and the peak becomes wider.

Next, we examined the effect of changing opacity (Fig. 3d). The chosen values of this parameter were 0.2, 0.3, and 0.4 cm^2/g. Decreasing opacity results in rising luminosity and shorter plateau phase.

To test the magnetar energy input, the initial rotational energy of the magnetar were set as 0.01, 0.1, and 1 foe. As Fig. 4a shows, this parameter has significant influence on the entire light curve. Higher E_p results in rising luminosities and broader plateau phase. If the initial rotational energy is not comparable to the recombination energy, no recognizable plateau phase is created by the magnetar energy input.
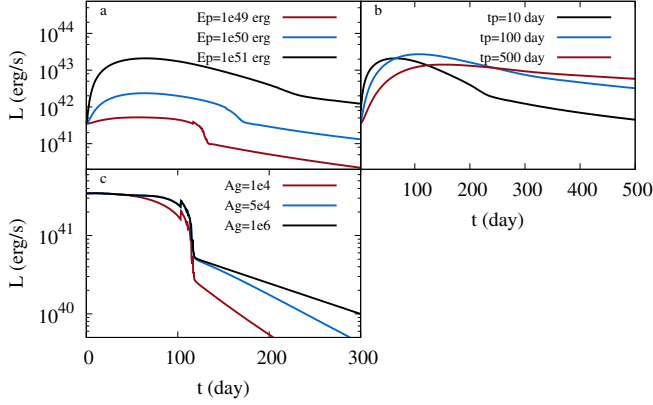
Fig. 4. Effect of changing the initial rotation energy of the magnetar (panel **a**)), the characteristic timescale of magnetar spin-down (panel **b**)), the gamma-ray leakage exponent (panel **c**)).

The characteristic timescale of the spin-down was chosen as t_p = 10, 100, and 500 days. The light curve strongly depends on the ratio of the effective diffusion time and spin-down timescale (Fig. 4b). As far as t_p is well below t_d, increasing spin-down time causes higher luminosities and wider plateau phase, but if $t_p \gg t_d$, the maximum starts to decrease. In this particular case $t_d \sim$ 97.35 days was applied.

Finally, the gamma-ray leakage exponent was varied as 10^4, 5×10^4, and 10^6 day^2. Figure 4c shows the strong influence of this parameter on the entire light curve. The tail luminosity is significantly related to the gamma-ray leakage, as expected. Increasing A_g results in a wider plateau phase, and also increases the tail luminosity.

To summarize the results of these tests, we conclude that:

a) the duration of the plateau phase is strongly influenced by the values of the initial radius of the ejecta, the ejected mass, the density profile exponent, and the kinetic energy;

b) the opacity, the initial nickel mass, and the recombination temperature are weakly correlated with the duration of the plateau;

c) the maximum brightness and the form of the peak mainly depend on the thermal energy, the initial nickel mass, the initial radius of the ejecta, the density profile exponent, and the magnetar input parameters;

d) the peak luminosity of the plateau is weakly influenced by the ejected mass and the opacity;

e) the late light curve is determined by the amount of the initial nickel mass, the gamma-ray leakage exponent, and the characteristic features of the magnetar; and

f) the light curve is less sensitive to the recombination temperature and opacity.

These results are generally in very good agreement with the conclusions by Arnett & Fu (1989) regarding the behavior of the initial radius, the recombination temperature and the factor $\kappa\ M_{ej}/v_{sc} \approx \kappa\ M_{ej}/\sqrt{E_{SN}/M_{ej}}$. Furthermore, our results show the same parameter dependence of the plateau duration as calculated by Popov (1993).

2.3. Parameter correlations

The correlation between parameters as examined by the Pearson correlation coefficient method, which measures the linear correlation between two variables. For this comparison, we first synthesized a test light curve for both the radioactive decay and
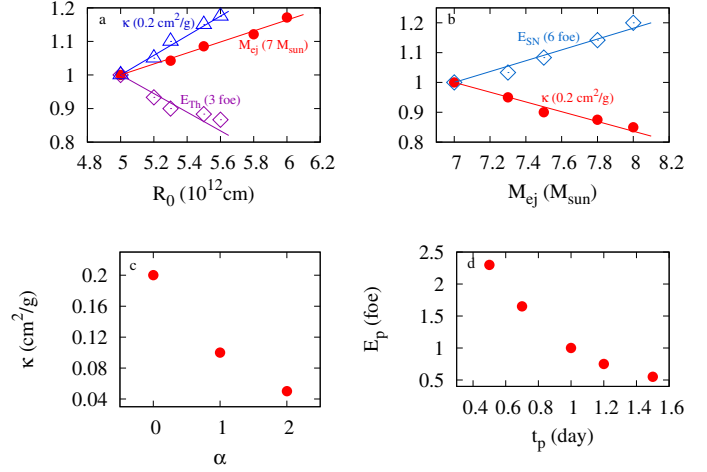

Fig. 5. Scatter diagrams of the correlated parameters. Panel **a**): κ (in 0.2 cm^2/g), M_{ej} (in 7 $M_\odot$), and E_{Th} (in 3 foe) vs. R_0; panel **b**): E_{SN} (in 6 foe) and κ (in 0.2 cm^2/g) vs. M_{ej}; panel **c**): κ vs. α; Panel **d**): E_p vs. t_p.

magnetar-controlled energy input models. Then, we tried each parameter-combination to create the same light curve and determine the correlations among the parameters. The scatter diagrams (Fig. 5) illustrate this correlation between the two particular parameters: if the general shape of the distribution of random parameter choices shows a trend, the parameters are more correlated.

The final result shown in Fig. 5 suggests that only three of the parameters are independent, T_{rec}, M_{Ni}^0, and A_g, while the other parameters are more or less correlated with each other.

3. Comparison with observations and hydrodynamic models

In this section, we compare the parameters calculated from our radioactive energy input models with those from hydrodynamic simulations. We fit SNe 2004et, 2005cs, 2009N, 2012A, and 2012aw using our code using the radioactive energy input. Since our simple code is unable to capture the first post-breakout peak, the comparison between the data and the model was restricted to the later phases of the plateau and the radioactive tail.

Like most other SN modeling codes, our code needs the bolometric light curve, which is not observed directly. In order to assemble the bolometric light curves for our sample we applied the following steps. First, the measured magnitudes in all available photometric bands were converted into fluxes using proper zero points (Bessell et al. 1998), extinctions, and distances. The values of extinction in each case were taken from the NASA/IPAC Extragalactic Database (NED). At epochs when an observation with a certain filter was not available, we linearly interpolated the flux using nearby data. For the integration over wavelength, we applied the trapezoidal rule in each band with the assumption that the flux reaches zero at 2000 Å. The infrared contribution was taken into account by the exact integration of the Rayleigh-Jeans tail from the wavelength of the last available photometric band (I or K) to infinity.

Note that to obtain a proper comparison with the other models collected from literature, we calculated the bolometric light curve using the same distance as in the reference papers.

Table 2. Results for SN 2004et.

Parameter	This paper	Literature	
		Model A[1]	Model B[2]
R_0 [10^{13} cm]	4.2	4.39	10.4
M_{ej} [$M_\odot$]	11.0	14.0	22.9
M_{Ni} [$M_\odot$]	0.060	0.060	0.068
E_{tot} [10^{51} erg]	1.95	0.88	2.30

References. [1] Maguire et al. (2010); [2] Utrobin & Chugai (2009).
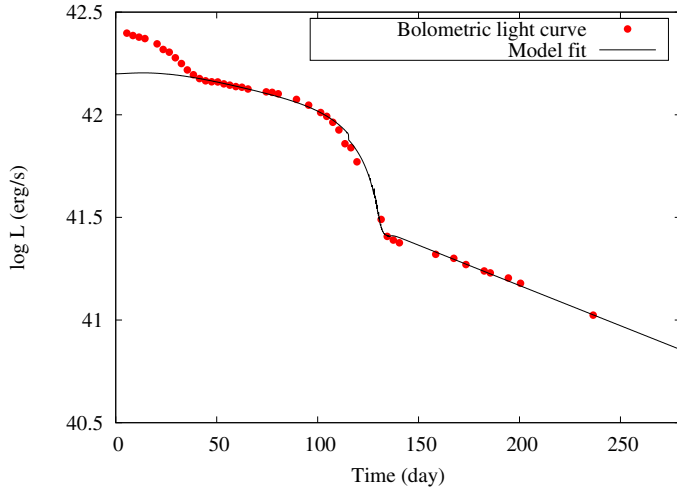
Fig. 6. Light curve of SN 2004et (dots) and the best result of our model (solid line).

3.1. SN 2004et

SN 2004et was discovered on 2004 September 27 by S. Moretti (Zwitter & Munari 2004). It exploded in a nearby starburst galaxy NGC 6946 at a distance of about 5.9 Mpc. This was a very luminous and well-observed Type IIP supernova (Sahu et al. 2006) in optical (*UBVRI*) and NIR (*JHK*) wavelengths. In this paper, all of these photometric bands were used to derive the bolometric light curve.

In the literature, SN 2004et was modeled with different approaches. Utrobin & Chugai (2009) used a 1-dimensional hydrocode to estimate the progenitor mass and other physical properties. Maguire et al. (2010) applied the formulae by Litvinova & Nadyozhin (1985) that are based on their hydrodynamical models, and also used the steepness parameter method from Elmhamdi et al. (2003), to get the physical parameters of SN 2004et. Table 2 shows the parameters from Maguire et al. (2010) and Utrobin & Chugai (2009) as well as our best-fit results. The bolometric light curve of SN 2004et and the model curve fitted using our code are plotted in Fig. 6.

3.2. SN 2005cs

The underluminous supernova SN 2005cs was discovered on 2005 June 30 in M51 by Kloehr (2005). This event was more than a magnitude fainter than an average Type IIP supernova. Nevertheless, the light curve of SN 2005cs was observed in *UBVRI* bands and its physical properties were calculated by Tsvetkov et al. (2006) based on the hydrodynamic model of Litvinova & Nadyozhin (1985). SN 2005cs was also fitted using our code and the results can be found in Table 3. For better comparison, we used d = 8.4 Mpc for the distance of M51,

Table 3. Results for SN 2005cs.

Parameter	This paper		Literature[1]
	d = 7.1 Mpc	d = 8.4 Mpc	
R_0 [10^{13} cm]	1.20	1.50	1.22
M_{ej} [$M_\odot$]	8.00	8.00	8.61
M_{Ni} [$M_\odot$]	0.002	0.003	0.0018
E_{tot} [10^{51} erg]	0.48	0.5	0.3

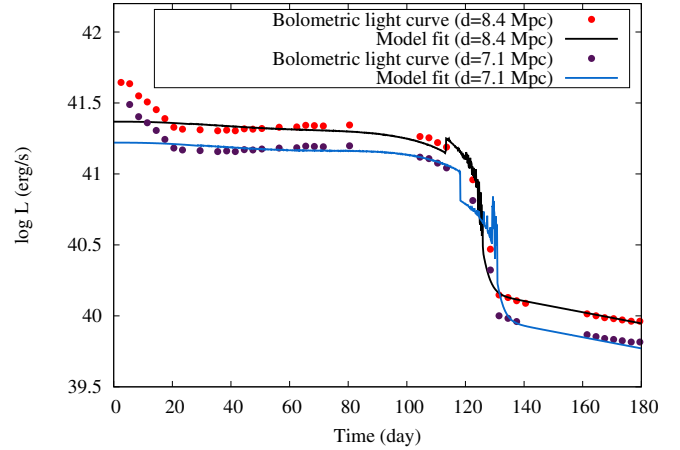**References.** [1] Tsvetkov et al. (2006).

Fig. 7. Best fit for SN 2005cs (black line) and the bolometric luminosity at 8.4 Mpc (red dots). The orange circles represent the light curve of SN 2005cs at 7.1 Mpc and the gray line is our fit.

Table 4. Results for SN 2009N.

Parameter	This paper	Literature[1]
R_0 [10^{13} cm]	1.60	2.00
M_{ej} [$M_\odot$]	7.6	11.5
M_{Ni} [$M_\odot$]	0.016	0.02
E_{tot} [10^{51} erg]	0.8	0.48

References. [1] Takáts et al. (2014).

which was adopted by Tsvetkov et al. (2006). However, we also calculated the quasi-bolometric light curve with d = 7.1 Mpc (Takáts & Vinkó 2006). The results for both distances are listed in Table 3. The best fit of our model can be seen in Fig. 7.

3.3. SN 2009N

SN 2009N was discovered in NGC 4487 having a distance of 21.6 Mpc (Takáts et al. 2014). The first images were taken by Itagaki on 2009 Jan. 24.86 and 25.62 UT (Nakano et al. 2009). This event was not as luminous as a normal Type IIP SN, but it was brighter than the underluminous SN 2005cs. Hydrodynamic modeling was presented by Takáts et al. (2014) who applied the code of Pumo et al. (2010) and Pumo & Zampieri (2011). In Table 4, we summarize our results as well as the properties from hydrodynamic simulations. Figure 8 shows the luminosity from the observed data and the model light curve.

3.4. SN 2012A

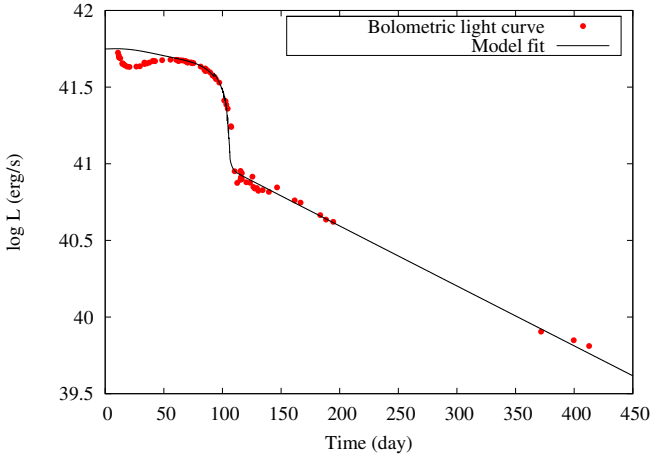SN 2012A was discovered in an irregular galaxy NGC 3239 at a distance of 9.8 Mpc (Tomasella et al. 2013). The first

Fig. 8. Solid line shows the fit of our model and the dots represent bolometric luminosity from observed data of SN 2009N.

Table 5. Results for SN 2012A.

Quantity	This paper	Literature[1]
R_0 [10^{13} cm]	1.8	1.8
M_{ej} [$M_\odot$]	8.80	12.5
M_{Ni} [$M_\odot$]	0.01	0.011
E_{tot} [10^{51} erg]	0.8	0.48

References. [1] Tomasella et al. (2013).
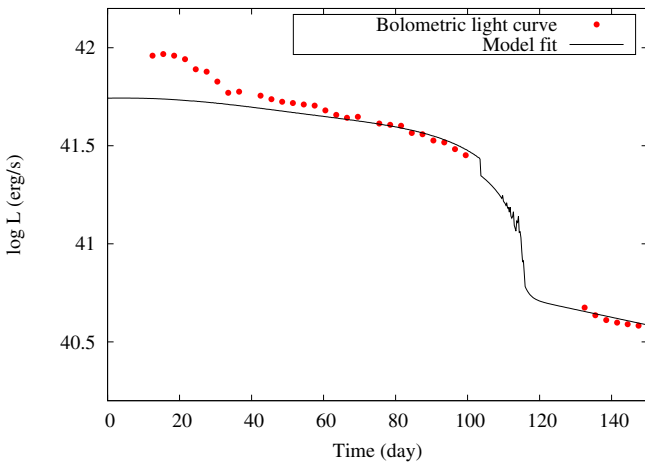
Fig. 9. Light curve of SN 2012A (dots) and the best result of our model (solid line).

image was taken on 2012 Jan. 7.39 UT by Moore, Newton & Puckett (2012). This event was classified as a normal Type IIP supernova with a short plateau. The luminosity drop after the plateau was intermediate between those of normal and underluminous Type IIP SNe. The fact that SN 2012A exploded in a nearby galaxy made this object very well-observed in multiple (*UBVRIJHK*) bands. For computing the physical properties of the progenitor, Tomasella et al. (2013) applied a semianalytical (Zampieri et al. 2003) and a radiation-hydrodynamic code (Pumo et al. 2010; Pumo & Zampieri 2011). Table 5 contains the final results of Tomasella et al. (2013) and our fitting parameters as well. Our model light curve can be seen in Fig. 9.

Table 6. Results for SN 2012aw.

Quantity	This paper	Literature[1]
R_0 [10^{13} cm]	2.95	3.0
M_{ej} [$M_\odot$]	20.0	20.0
M_{Ni} [$M_\odot$]	0.056	0.056
E_{tot} [10^{51} erg]	2.2	1.5

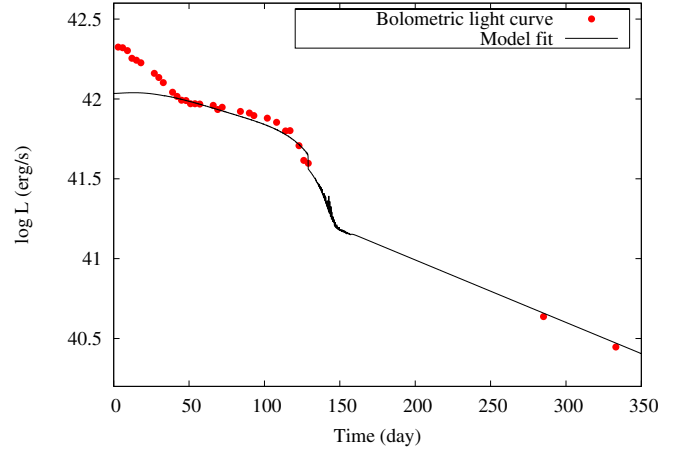**References.** [1] Dall'Ora et al. (2014).

Fig. 10. Light curve of SN 2012aw (dots) and the best result of our model (solid line).

3.5. SN 2012aw

SN 2012aw was discovered on 2012 March 16.86 UT by P. Fagotti (Fagotti et al. 2012) in a spiral galaxy M95 at an average distance of 10.21 Mpc. This was a very well-observed Type IIP supernova in optical (*UBVRI*) and NIR (*JHK*) wavelengths (Dall'Ora et al. 2014). All of these photometric bands were used to create the bolometric light curve.

The physical properties of SN 2012aw modeled by Dall'Ora et al. (2014) who applied two different codes: a semianalytic (Zampieri et al. 2003) and a radiation-hydrodynamic code (Pumo et al. 2010; Pumo & Zampieri 2011). In Table 6 we summarize our result as well as the parameter values of Dall'Ora et al. (2014). Our best-fit model is plotted in Fig. 10.

4. Discussion and conclusion

The good agreement between the results from the analytical light curve modeling and the parameters from other hydrodynamic calculations leads to the conclusion that the usage of the simple analytical code may be useful for preliminary studies prior to more expensive hydrodynamic computation. The code described in this paper is also capable of providing quick estimates for the most important parameters of SNe such as the explosion energy, the ejected mass, the nickel mass, and the initial radius of the progenitor from the shape and peak of the light curve as well as its late-phase behavior. Note that there is a growing number of observational evidence showing that the plateau durations have a narrow distribution with a center at about 100 days (Faran et al. 2014), which suggests that strong correlations exist between parameters like the explosion energy and the progenitor radius in the presupernova stage. The code may offer a fast and efficient way to explore such type of parameter correlations.

Tables 2–6 show that the hydrodynamic models for Type IIP events consistently give higher ejected masses than our code.

On the other hand, there are also major differences between the values given by different hydrocodes, such as in the case of SN 2004et. Although the total SN energies from our code are usually higher then those obtained from more complex models, they show a similar trend: for an underluminous SN the best-fit energy is lower, while for a more luminous SN the code suggests higher explosion energy.

The present code has various limitations and caveats. One of them is that it is not able to fit the light curve at very early epochs. This may be explained by the failure of the assumption of homologous expansion at such early phases, and/or the adopted simple form of the density profile. Another possibility could be the assumption of a two-component ejecta configuration, which is sometimes used for modeling Type IIb SNe (Bersten et al. 2012). In this case, the model also contains a low-mass envelope on top of the inner, more massive core. Within this context the fast initial decline may be due to radiation diffusion from the fast-cooling outer envelope heated by the shock wave due to the SN explosion. These models will be studied in detail in a forthcoming paper.

References

Arnett, W. D. 1980, ApJ, 237, 541
Arnett, W. D. 1982, ApJ, 253, 785
Arnett, W. D., & Fu, A. 1989, ApJ, 340, 396
Bessell, M. S., Castelli, F., & Plez, B. 1998, A&A, 333, 231
Blinnikov, S., Lundqvist, P., Bartunov, O., et al. 2000, ApJ, 532, 1132
Bersten, M. C., Benvenuto, O., & Hamuy, M. 2011, ApJ, 729, 61
Bersten, M. C., Benvenuto, O. G., Nomoto, K., et al. 2012, ApJ, 757, 31
Chatzopoulos, E., Wheeler, J. C., & Vinkó, J. 2012, ApJ, 746, 121
Dall'Ora, M., Botticella, M. T., Pumo, M. L., et al. 2014, ApJ, 787, 139
Elmhamdi, A., Chugai, N. N., & Danziger, I. J. 2003, A&A, 404, 1077
Fagotti, P., Dimai, A., Quadri, U., et al. 2012, CBET, 3054, 1
Falk, S. W., & Arnett, W. D. 1977, ApJS, 33, 515
Faran, T., Poznanski, D., Filippenko, A. V., et al. 2014, MNRAS, 442, 844
Grassberg, E. K., & Nadyozhin, D. K. 1976, Ap&SS, 44, 409
Grassberg, E. K., Imshennik, V. S., & Nadyozhin, D. K. 1971, Ap&SS, 10, 28
Hatano, K., Branch, D., Fisher, A., et al. 1999, ApJS, 121, 233
Hillebrandt, W., & Müller, E. 1981, A&A, 103, 147
Kasen, D., & Bildsten, L. 2010, ApJ, 717, 245
Kloehr, W. 2005, IAU Circ., 8553, 1
Litvinova, I. Y., & Nadyozhin, D. K. 1985, Sov. Astron. Lett., 11, 145
Maguire, K., Di Carlo, E., Smartt, S. J., et al. 2010, MNRAS, 404, 981
Moore, B., Newton, J., & Puckett, T. 2012, CBET, 2974, 1
Nadyozhin, D. K. 2003, MNRAS, 346, 97
Nakano, S., Kadota, K., & Buzzi, L. 2009, CBET, 1670, 1
Piro, A. L., & Ott, C. D. 2011, ApJ, 736, 108
Popov, D. V. 1993, ApJ, 414, 712
Pumo, M. L., & Zampieri, L. 2011, ApJ, 741, 41
Pumo, M. L., Zampieri, L., & Turatto, M. 2010, MSAIS, 14, 123
Sahu, D. K., Anupama, G. C., Srividya, S., et al. 2006, MNRAS, 372, 1315
Takáts, K., & Vinkó, J. 2006, MNRAS, 372, 1735
Takáts, K., Pumo, M. L., Elias-Rosa, N., et al. 2014, MNRAS, 438, 368
Tomasella, L., Cappellaro, E., Fraser, M., et al. 2013, MNRAS, 434, 1636
Tsvetkov, D. Y., Volnova, A. A., Shulga, A. P., et al. 2006, A&A, 460, 769
Utrobin, V. D. 2007, A&A, 461, 283
Utrobin, V. D., & Chugai, N. N. 2009, A&A, 506, 829
Utrobin, V. D., Chugai, N. N., & Pastorello, A. 2007, A&A, 475, 937
Woosley, S. E. 2010, ApJ, 719, L204
Zampieri, L., Pastorello, A., Turatto, M., et al. 2003, MNRAS, 338, 711
Zwitter, T., & Munari, U. 2004, IAU Circ., 8413, 1